JGR Space Physics

Short-Wavelength Electrostatic Wave Measurement Using MMS Spacecraft

Ahmad Lalti[1,2] , **Yuri V. Khotyaintsev**[1] , and **Daniel B. Graham**[1]

[1]Swedish Institute of Space Physics, Uppsala, Sweden, [2]Space and Plasma Physics, Department of Physics and Astronomy, Uppsala University, Uppsala, Sweden

Abstract Determination of the wave mode of short-wavelength electrostatic waves along with their generation mechanism requires reliable measurement of the wave electric field. We show that for such waves the electric field measured by Magnetospheric MultiScale becomes unreliable when the wavelength is close to the probe-to-probe separation. We develop a method, based on spin-plane interferometry, to reliably determine the full three-dimensional wave vector of the observed waves. We test the method on synthetic data and then apply it to ion acoustic wave bursts measured in the solar wind. By studying the statistical properties of ion acoustic waves in the solar wind, we retrieve the known results that the wave propagation is predominantly field aligned. We also determine the wavelength of the waves. We find that the nominal value is around 100 m, which when normalized to the Debye length corresponds to scales between 10 and 20 Debye lengths.

1. Introduction

Most plasma environments in space are collisionless (Baumjohann & Treumann, 2012), which means that inter-particle collisions do not play any significant role in the dynamical evolution of the system. In such a case, and if we ignore the effect of gravitational forces, long range electromagnetic forces govern the dynamics of the plasma. One of the open questions in space plasma physics is the question of irreversible energy dissipation without collisions. It is believed that short-wavelength electrostatic waves, through wave-particle interactions, play a key role in creating such irreversible dissipation whether at collisionless shocks (Sagdeev, 1966; Wilson et al., 2014a, 2014b), at magnetic reconnection (Khotyaintsev et al., 2019) or at terminating the energy cascade in plasma turbulence (Valentini & Veltri, 2009; Valentini et al., 2008, 2014). The exact channels with which such waves dissipate energy are still under investigation.

The study of short-wavelength electrostatic waves in space plasmas requires reliable measurement of the wave electric field. Several techniques have been developed for measuring it (Mozer, 1973). One widely used technique is the double-probe technique (Fahleson, 1967; Pedersen et al., 1998), where the electric field is estimated by taking the difference between the probe to spacecraft potential measured at two points in space, then dividing by the probe-to-probe separation

$$E_{ij} = -\frac{V_i - V_j}{d_{ij}} \tag{1}$$

where the indices refer to the measurement points (i.e., the probes), E_{ij} is the electric field pointing from probe j to probe i and d_{ij} is the separation distance between probes i and j. The first electric field measurement based on the double-probe technique was performed in 1967 on a sounding rocket flown to the auroral ionosphere (Mozer & Bruston, 1967). Following this success the double-probe technique has been and is currently being used on multiple spacecraft throughout the heliosphere such as the Van Allen probes (Wygant et al., 2013), THEMIS (Bonnell et al., 2009), Cluster (Gustafsson et al., 1997), and Solar Orbiter (Maksimovic et al., 2020) to name a few.

This technique is also operated on the Magnetospheric MultiScale (MMS) mission (Burch et al., 2016). MMS is a constellation of four spacecraft in a tetrahedral formation equipped with high temporal and spatial resolution particles and fields instruments allowing scientists to probe kinetic scale space plasma phenomena. The electric field double-probe (EDP) instrument aboard MMS consists of two orthogonal spin-plane double probes (SDP) (Lindqvist et al., 2016) with probe-to-probe distance of 120 m, and axial double probes (Ergun et al., 2016) with probe-to-probe distance of 28.15 m. The set of six probes enables the measurement of the three-dimensional (3D)

electric field from DC up to 128 kHz. Since its launch in 2015, many studies have used the EDP data from MMS to study plasma wave phenomena in the various plasma regions around Earth from the bow shock (Goodrich et al., 2018; Vasko et al., 2018, 2022; Wang et al., 2021) to the magnetopause (Graham et al., 2022; Khotyaintsev et al., 2020; Steinvall et al., 2019) to the magnetotail (Le Contel et al., 2017; Richard et al., 2021).

Despite this success, measurement of wave electric fields with wavelength comparable to the probe-to-probe distance ($\sim 10^2$ m) can become unreliable (LaBelle & Kintner, 1989). That is why there is a need to test the performance of the EDP instrument when it comes to measuring such waves, and understand what effects can affect the electric field measurement. Then develop a method to mitigate those problems to give reliable measurement of the plasma wave properties. In Section 2 of this paper, we use electrostatic waves whose properties are generally known, namely ion acoustic waves in the solar wind, to test the performance of the EDP instrument on MMS. In Section 3, we develop a method to mitigate the problems identified in Section 2 and reliably measure the full 3D wave vector of the observed waves. In Section 4, we use this method to conduct a case study of one ion acoustic wave bursts with peculiar power spectral density (PSD) signature. We also study statistically the properties of those waves. Finally, in Section 5, we summarize and conclude.

2. Short-Wavelength Electric Field Measurement by MMS

In order to test the performance of MMS when it comes to measuring short-wavelength electrostatic waves, we need to use waves whose characteristics and properties, namely angle of propagation with the background magnetic field, θ_{kB}, wavelength, and frequency, are well known. One such wave mode is the ion acoustic waves in the solar wind (Gurnett & Anderson, 1977; Gurnett & Frank, 1978; Mozer et al., 2020; Píša et al., 2021). Many studies have shown that those waves propagate predominantly in a field-aligned direction; e.g., recently Píša et al. (2021) used the Solar Orbiter spacecraft to study ion acoustic waves in the solar wind and found that 80% of their observed waves have a θ_{kB} less than or equal to 20°. Furthermore, due to their short wavelength, ion acoustic waves in the solar wind can be highly Doppler shifted, so their observed frequency in the spacecraft frame can range from a few hundred to thousands of Hz.

We compile a set of 210 ion acoustic wave bursts observed with MMS in the quiet undisturbed solar wind. When compiling the list of wave bursts we make sure that the spacecraft was not in the ion or electron foreshock by excluding intervals showing electrostatic wave activity characteristic of such regions. We do so by inspecting the PSD data product, which resolves frequencies reaching 100 kHz but sampled at lower temporal resolutions. We also make sure that we do not have any Langmuir waves present in the time interval. This way we make sure that the most likely observed wave mode is indeed ion acoustic waves (Gurnett & Frank, 1978).

An example of an ion acoustic wave burst observed by MMS1 is shown in Figure 1. Panel (a) shows the PSD of the electric field showing the peak frequency around 1.5 kHz. Panel (b) shows the electric field as measured using the double-probe technique (Equation 1), and expressed in the probes coordinate system (PCS) (see Figure 3a) where the positive x is along probe 1, positive y is along probe 3, positive z is along probe 5. Panel (c) of Figure 1 shows the electric field rotated into the coordinate system defined by the minimum, intermediate, and maximum variance directions (Paschmann & Daly, 1998; Sonnerup & Scheible, 1998). The maximum variance direction of this wave burst is $\hat{\mathbf{k}}_{max} = [0.26, 0.41, 0.87]$, with a large component in the z direction. With a background magnetic field direction of $\hat{\mathbf{b}} = [0.67, 0.52, 0.53]$ we obtain $\theta_{kB} = 31°$, which is relatively oblique compared to what is statistically expected in the solar wind. Having no wave activity near the plasma line (not shown), the only wave mode that fits the characteristics for this event is that of oblique ion acoustic waves.

Three effects can possibly affect the electric field measurement derived from the double-probe technique. The first is the sheath impedance effects (Gurnett, 1998; Hartley et al., 2016). The probes are not directly coupled to the plasma; a sheath forming around the probe causes a potential drop between the plasma and the surface of the probe. In a circuit diagram this sheath can be modeled as a capacitor and resistor connected in parallel between the plasma and the probes (see e.g., Figure 5 in Hartley et al. (2016)). This parallel RC circuit has a voltage divider effect on the probe with complex impedance, $V_{in}/V_{out} = \frac{Z_L}{Z_s + Z_L}$ where V_{in} is the plasma potential, V_{out} is the measured potential, and Z_L/Z_s are the load (spacecraft)/sheath impedances, respectively. At low frequencies (compared to the characteristic RC time of the circuit), the probe is resistively coupled to the plasma, and since by design the load resistance is much larger than any expected sheath resistance, the gain defined as the ratio V_{in}/V_{out} is close to 1. On the other hand, at higher frequencies, the probe is coupled capacitively to the plasma. In
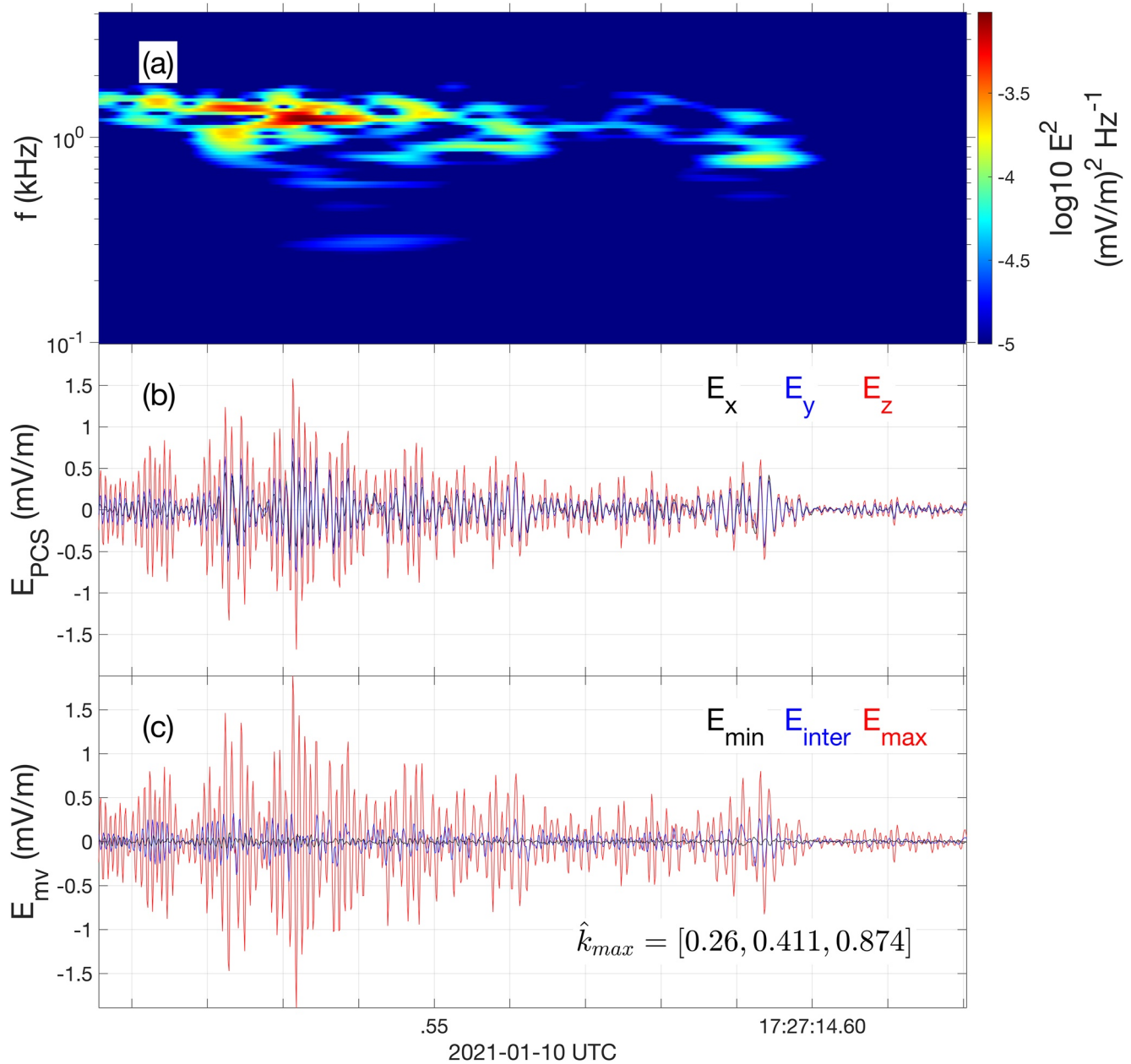
Figure 1. Example of an ion acoustic wave burst observed by MMS1 in the solar wind. Panel (a) shows the sum of the power spectral densities (PSDs) of the electric field components $E^2 = E_x^2 + E_y^2 + E_z^2$, (b) shows the electric field measured using the double-probe technique and set in the probes coordinate system (PCS), (c) shows the measured electric field rotated into the coordinate system defined by the minimum, intermediate, and maximum variance directions. Overlayed on panel (c) is the maximum variance direction in the PCS.

that limit, the gain is different from 1 so the measured electric field will exhibit both amplitude attenuation and phase shift (Hartley et al., 2016).

The second effect is the boom shorting effect (Califf & Cully, 2016; Pedersen et al., 1998). Both axial and spin-plane probes are connected to a preamplifier, which in turn is connected to the spacecraft by a long conducting wire boom. This boom is grounded to the spacecraft, so when an external electric field exists, it will induce a charge distribution on the surface of the spacecraft to satisfy the constant potential boundary condition. This will short out the external electric field causing a decrease in the amplitude of the measured electric field (Califf & Cully, 2016). This decrease in amplitude corresponds to d_{ij} in Equation 1 deviating from the physical probe-to-probe separation. So if one uses the physical probe-to-probe separation this will result in a decrease in

the measured amplitude otherwise an effective length rather than geometric length is required when calculating the electric field so the amplitude is not attenuated (Pedersen et al., 1998).

Finally, the third effect is the short-wavelength effect (Gurnett, 1998; LaBelle & Kintner, 1989) related to distortions to the wave amplitude and phase when the wavelength λ approaches the probe-to-probe separation scale. To illustrate the effect, we use synthetic data corresponding to a plane wave with the potential given by

$$V_w = V_0 \cos(\omega t - \mathbf{k} \cdot \mathbf{r}) \tag{2}$$

where ω is the frequency and $\mathbf{k}$ is the wavevector (with $k = \frac{2\pi}{\lambda}$). We assume the spacecraft is located at the origin, and thus the electric field of the wave is

$$\mathbf{E}_w = -\nabla V = -\mathbf{k}V_0 \sin(\omega t) \tag{3}$$

To simulate the double-probe measurement, we evaluate the potential (Equation 2) at the probe locations, and using Equation 1 calculate the corresponding components of the electric field $\mathbf{E}_{obs}$. We then calculate the attenuation factor $\alpha = E_{ij}/E_w$, which is plotted in Figure 2a, where $\mathbf{k}$ is aligned with the probe pair $i - j$. We observe $\alpha \sim 1$ at long wavelengths (large λ/d_{ij}); α decreases as λ approaches the probe-to-probe separation d_{ij}, until it reaches zero at $\lambda/d_{ij} = 1$; it then oscillates between positive values and zero for $\lambda/d_{ij} < 1$. Similar behavior is seen in the phase shift $\Delta\Phi$ between E_{ij} and E_w shown in panel (b); $\Delta\Phi$ is close to zero for $\lambda/d_{ij} \gg 1$, and increases with decreasing λ until it reaches π at $\lambda/d_{ij} = 1$. These results imply that the MMS double-probe measurements become unreliable (exhibit large distortions in phase and amplitude) for $\lambda \lesssim 50$ m for $\mathbf{k}$ close to the spin-axis direction, and $\lambda \lesssim 200$ m for $\mathbf{k}$ close to the spin plane.

By exploiting the asymmetry between the axial and spin-plane probes, we can use the angle that the vector electric field $\mathbf{E}$ makes with the z direction, θ_{Ez} (see Figure 3a), as an indicator of the instrument performance. The distribution of θ_{Ez} for every vector measurement of the 210 wave bursts (total of ~16,000 vectors) is shown in Figure 3b in black. The distribution is skewed toward small θ_{Ez} (peak at $\theta_{Ez} = 20°$) which indicates a possible problem with the measurement.

As the ion acoustic waves in the solar wind are predominantly field aligned, we can obtain a predicted distribution of θ_{Ez} based on the observed distribution of the angle θ_{Bz} between $\mathbf{B}$ and the spin-axis direction (shown in Figure 3c). We also take into account that the waves are not exactly field aligned but have a distribution in θ_{kB} (Píša et al., 2021). The obtained predicted distribution is shown in Figure 3b in green. Comparing it to the observed distribution (black), we confirm our suspicion of the problem with the measurement, i.e., that the electric field of short-wavelength waves measured by MMS is systematically shifted toward the axial direction. Thus, θ_{kB} we obtained earlier for the event shown in Figure 1 cannot be trusted.

We can model the instrument response due to the short-wavelength effect using synthetic data. We assume a distribution of plane ion acoustic waves (corresponding to the observed wave bursts) with the wave vector directions following the predicted θ_{Ez} distribution (green in Figure 3b). To obtain the wavelength, we assume a linear dispersion relation

$$\omega_{sc} = C_s k + \mathbf{V}_{sw} \cdot \mathbf{k} \tag{4}$$

where ω_{sc} is the measured frequency in the spacecraft frame, $C_s = \sqrt{\frac{k_B(T_e + 3T_i)}{M_p}}$ is the ion acoustic speed, $\mathbf{V}_{sw}$ is the solar wind velocity, $\mathbf{k}$ is the wave vector that we want to determine. The typical C_s in the solar wind at 1 AU is ~60 km/s (obtained using $T_e = 11.1$ and $T_i = 8.45$ eV (Wilson et al., 2021)) is much smaller than the typical solar wind speed. Thus, the Doppler term is the dominant in Equation 4, i.e., $\omega_{sc} \sim \mathbf{V}_{sw} \cdot \mathbf{k}$, except for the waves with $\mathbf{k}$ exactly perpendicular to $\mathbf{V}_{sw}$ (Gurnett, 1991). Therefore, we use $k = \omega_{sc}/V_{sw}$ to estimate the magnitude of the wave vector for each of the wave bursts in the distribution. Then, we compute the wave potential at the location of the probes using Equation 2 and the corresponding synthetic electric field, i.e., the field which would be measured by MMS, using Equation 1. We find an excellent agreement between the resulting synthetic distribution of θ_{Ez} (blue in Figure 3d) and the observed distribution (black). This indicates that the sheath impedance and boom shorting effects are of minor importance for the problem encountered, i.e., the skewness of the measured electric field toward the axial direction, and that the short-wavelength effect is its main cause.
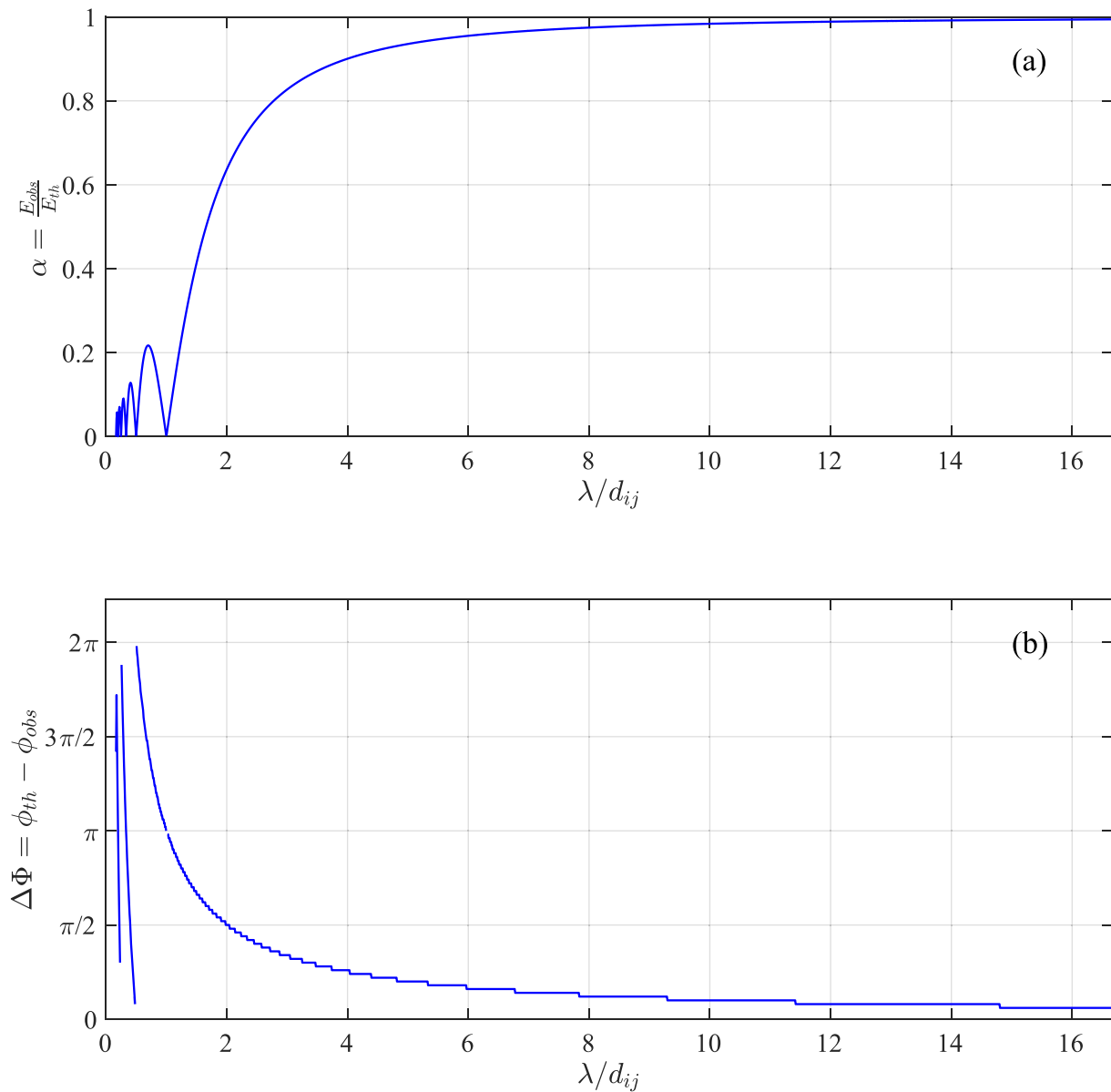
Figure 2. Predicted short-wavelength effects on double-probe electric field measurement. (a) The attenuation factor α and (b) the phase shift $\Delta\Phi$ versus the normalized wavelength λ/d_{ij}.

3. 3D Wave Vector Determination Using Spin-Plane Interferometry

In order to determine the wave mode of any wave burst, it is necessary to determine, in addition to its frequency, its direction of propagation and its wavelength. One of the easiest ways to get the direction of propagation of an electrostatic wave is by determining its maximum variance direction (Paschmann & Daly, 1998; Sonnerup & Scheible, 1998), as was done for the wave burst shown in Figure 1, which coincides with the direction of propagation of electrostatic waves (albeit with π ambiguity). But with the systematic shift of the electric field toward the axial direction shown in the previous section, the maximum variance direction of the electric field will not coincide with the direction of propagation of the wave, so there is a need for a reliable method to determine the wave properties despite the technical limitations described earlier.

In this section, we develop a method, based on the spin-plane multiprobe interferometry, to obtain the full 3D wave vector of any measured electrostatic short-wavelength wave burst.
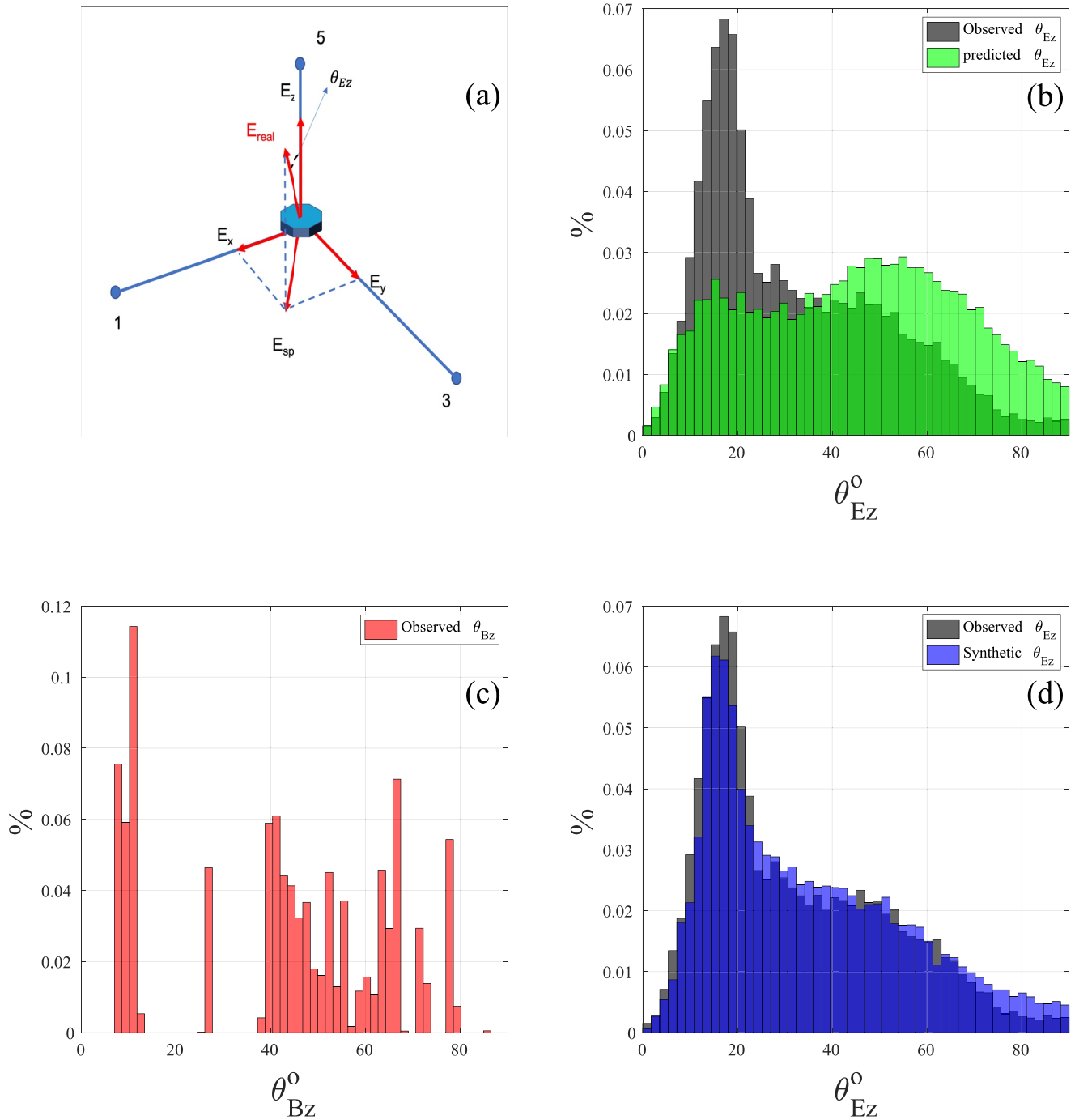
Figure 3. Systematic bias of the electric field measurement toward the axial probes direction. (a) Schematics of the probes coordinate system. (b) The observed, in black, and the expected, in green, θ_{Ez} distributions. (c) The distribution of the angle that the magnetic field makes with the axial direction θ_{Bz} in red. (d) The observed in black, and the synthetic, in blue, θ_{Ez} distributions.

1. We first calculate the frequency dependent wave vector in the spin plane using spin-plane interferometry.
2. We then use this result to correct for the attenuation effect in the spin-plane components of the electric field.
3. We calculate the maximum variance direction of the corrected electric field and use it to determine the frequency dependent 3D wave vector.
4. By synthetically generating a plane wave at different propagation directions and different wavelengths and then applying the steps described above to measure the synthetic wave properties, we obtain a look-up table
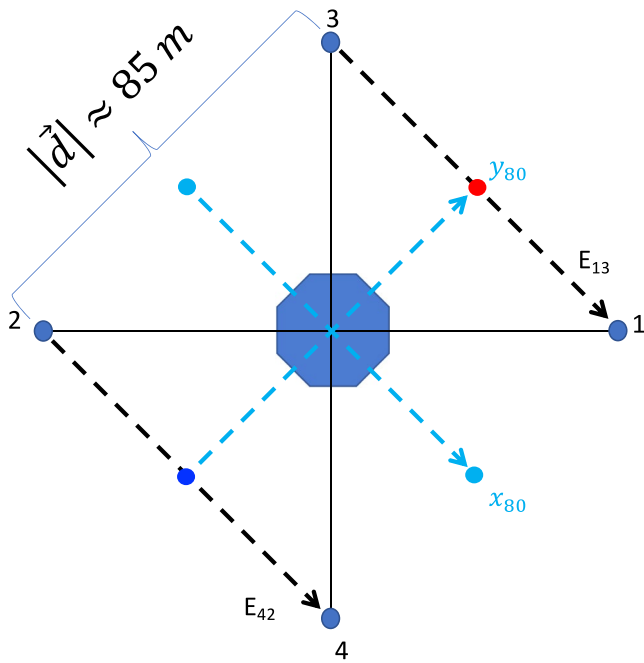
Figure 4. Schematics of the spin-plane probes showing the two orthogonal directions along which interferometry is applied, forming the E80 coordinate system.

that allows us to determine the actual wavelength and propagation direction of a wave from its measured properties.

In the following sections, we provide a detailed description of each step of the method.

3.1. Spin-Plane Wave Vector Determination

One powerful method that can be used to determine the wave vector is single spacecraft interferometry. This method has been used before in analyzing short scale waves from various spacecraft and throughout the heliosphere (Balikhin et al., 2005; Bonnell et al., 1996; Graham et al., 2016; Khotyaintsev et al., 2010; Vaivads et al., 2004; Vasko et al., 2018, to cite a few). The method works by measuring the same quantity (electric field, probe potential, density, etc.) at two different locations in space. When a localized structure or a plane wave passes the spacecraft, it will leave a signature in the measured quantity at one location and then at the other depending on its direction of propagation. By measuring the time delay Δt (or equivalently the phase shift $\Delta\phi$) between the two measurements and knowing the distance between the two measurement points **d**, one can determine the wave vector (**k**) in the direction of the two measurement points using

$$\mathbf{k} \cdot \mathbf{d} = \Delta\phi \tag{5}$$

For electrostatic waves measured by MMS, one can apply interferometry on both the probe potentials or electric fields. Using synthetic data, Steinvall et al. (2022) found that one particular electric field configuration, what they call "diagonal electric field" and what we will call E80 electric field, is the most reliable quantity to apply interferometry on. In order to explain the E80 interferometry, we show in Figure 4 a schematic of MMS in the spin plane, using probes 2 and 4 we calculate the electric field E_{42}, and using probes 3 and 1 we calculate the electric field E_{13}. Those two electric fields are the same field components measured at two different spatial locations (the dark blue and red circles in the schematics) separated by a distance $d_{80} \approx 85$ m. So by measuring the phase shift between the two measurements, one can use Equation 5 to obtain the wave vector component in the direction named y_{80} in Figure 4. The same thing can be applied to the orthogonal direction where phase shifts between electric fields E_{32} and E_{14} can be used to obtain the component of the wave vector in the direction named x_{80} in Figure 4. Using this method, one obtains the spin-plane wave vector components. It is worth noting that those two directions (x_{80} and y_{80}) define a coordinate system (which we will call E80 coordinate system) that is rotated by 45° clock-wise from the coordinate system aligned with the two wire boom pairs (PCS).

Note that there is a small time delay between the measurement of the potential by the six probes. We correct for this delay and then resample the measurements to the timeline of probe 1.

Unfortunately, the E80 interferometry technique is restricted to the spin plane, so we cannot use it to get the axial component of the wave vector. Other quantities can be timed in the axial direction, such as the potential measured at probes 5 and 6, but such timing is often unreliable (Steinvall et al., 2022).

Before going in to the 3D wave vector determination, it is informative to see the spin-plane interferometry technique in action. And before applying to real data, we use synthetic data. We generate a wave packet comprised of a sum of sinusoidal waves all traveling in the same direction at a polar angle $\theta = 60°$ and an azimuthal angle $\phi = 30°$ in the PCS. The waves have frequencies that are logarithmically spaced between 100 Hz and 3.5 kHz, and follow the dispersion relation:

$$f = V_{ph}k/(2\pi) = V_{ph}/\lambda \tag{6}$$

where V_{ph} is a constant representing the phase velocity of the waves. Throughout this paper in our synthetic wave packet, we use V_{ph} to be equal to 90 km/s giving a range of wavelength $\lambda \in [25\ 900]$ m and wavenumber $k \in [0.007\ 0.2477]$ m^{-1}. The potential of the full wave packet has the functional form

$$V(\mathbf{r}, t) = \sum_i V_0 \cos(\omega_i t - \mathbf{k}_i \cdot \mathbf{r}) \tag{7}$$

where the sum is over all frequency components, $\mathbf{k}$ is the wave vector, $\mathbf{r} = (x, y, z)$ is the position vector, and V_0 is a constant amplitude.

We evaluate the potential of this wave packet at six different spatial locations that coincide with the location of probes 1 through 6. In order to apply interferometry for the spin-plane components of the electric field and for all the frequency components in the wave packet, we apply a wavelet transform on the electric fields (E_{42} and E_{13} to get the wave vector in the y_{80} direction and E_{32} and E_{14} to get the wave vector in the x_{80} direction). In the wavelet space, we can calculate the phase difference between the two signals, $\Delta\phi$ (Equation 2 in Graham et al. (2016)), and calculate a wavenumber at each frequency using Equation 5 and each time step. Then we bin the power in frequency-wavenumber ($f - k$) space by summing the power of every measurement point that has $f - k$ values within each bin. The resulting $f - k$ power spectrum for both E80 directions is shown in Figures 5a and 5b. Those panels show a clear linear dispersion relation marked out with the high values of the PSD.

Interferometry works well for wavelengths larger than twice the distance between the two measurement points, in our case $\lambda > 2 \times d_{80} = 2 \times 85 = 170$ m. Or in terms of the wavenumber $k_{x,y} = 0.037$ m^{-1} where $k_{x,y}$ is the wavenumber in the x/y direction. When the wavelength becomes <170 m the measurement will be subject to spatial aliasing. In $f - k$ space aliasing causes the signal to wrap around to the opposite limit of the domain as is seen in panels (a and b) of Figure 5, when the wavenumber approaches the limiting value of 0.037 the dispersion relation continues from the -0.037 value and the same behavior repeats with every encounter of the dispersion relation with the edge of the $k_{x,y} = [-0.037\ 0.037]$ m^{-1} domain. This effect can easily be mitigated by extending the $k_{x,y}$ domain as is done in panels (c and d), we see how the continuous linear dispersion relation is retrieved. In both panels, we see multiple repeating branches. The branch that has a zero intercept (the branch that connects to $k = 0$) is the one that corresponds to the dispersion relation of the physical wave (Equation 4).

After having manually selected the appropriate branch and in order to retrieve a single dispersion relation at each frequency, we select values of k that correspond to the maximum power. The selected values are shown as black stars in panels (c and d) in Figure 5. Since the main coordinate system that we are using is the PCS, we rotate the spin-plane wave vector measured from the E80 to the probe coordinate system. In panel (e) of Figure 5, we plot the expected dispersion relation (Equation 6) projected along the x direction in the PCS in black. We overlay in red the dispersion relation obtained by the interferometry technique. We do the same in panel (b) but for the y direction. It is clear that after accounting for spatial aliasing we can retrieve the spin-plane dispersion relation of an observed wave packet down to wavelengths shorter than the length at which aliasing is expected to occur (170 m). It is worth noting that the dips in power seen in the PSD of Figure 5 (at $k_{x80} \sim 0.02$ (m^{-1}) in panel (a) and around frequencies 1 and 2.5 kHz in panel (c)) are due to frequencies where the projected wavelength along the probes direction is equal to the probe-to-probe separation of 120 m where we expect the attenuation factor α to be zero.

The conclusion from this subsection is that after accounting for the spatial aliasing in the way described one can reliably retrieve the spin-plane dispersion relation. This method works under one condition only, namely, the wave packet under investigation contains a significant spread in frequency and wavenumber to see a dispersion relation in the $f - k$ PSD in order to be able to select the correct branch that connects to the origin in $f - k$ space.

3.2. 3D Wave Vector Determination: Simulation

The E80 interferometry described in the previous section is a reliable method to determine the spin-plane components of the wave vector $\left(\vec{\kappa}(f_i) = \left[k_x(f_i),\ k_y(f_i)\right]\right)$. To calculate the component of $\mathbf{k}$ along the axial direction we develop the method detailed below:

1. Correct for the attenuation effect in the spin-plane components:
   - We calculate the electric field in the PCS ($\mathbf{E}$) such that: $E_x = -\frac{V_1 - V_2}{120}$, $E_y = -\frac{V_3 - V_4}{120}$, and $E_z = -\frac{V_5 V_6}{28.15}$.
   - Knowing the wavelength at each frequency f_i from the E80 interferometry, we determine the electric field amplitude attenuation factor $\alpha(f_i)$ by interpolating the values from the numerical relations shown in Figure 2a.
   - We Fourier transform the spin-plane components of $\mathbf{E}$ and we correct the amplitude by dividing it by the corresponding $\alpha(f_i)$. We then invert the Fourier transform to obtain a corrected electric field $\mathbf{E}_c$ (the spin-plane components corrected).
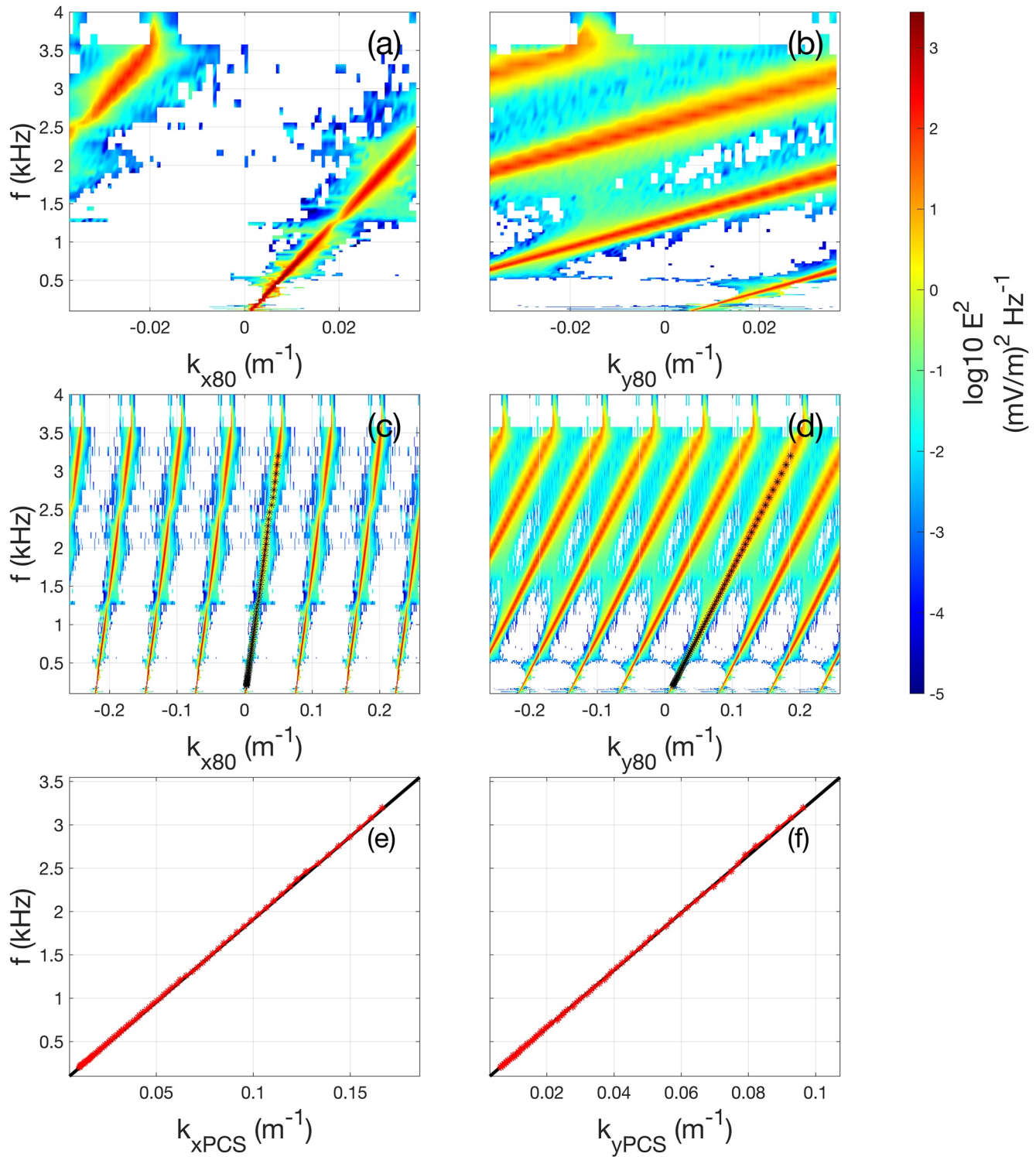
Figure 5. Results of spin-plane interferometry. Panels (a) and (b) show the $f - k$ power spectral density (PSD) in the x_{80} and y_{80} directions without accounting for aliasing. Panels (c) and (d) repeat what is plotted in (a) and (b) but after accounting for aliasing. Panels (e) and (f) show the theoretical (in black) and measured (in red) dispersion relations in the x_{PCS} and y_{PCS} directions.

2. Determine the direction of propagation of the wave at each frequency while accounting for the phase shift due to the attenuation effect:
   - The short-wavelength effect, as discussed in Section 2 (see Figure 2b), adds a spurious phase shift to the measured oscillating electric field compared to the real one. For each f_i, we band pass filter $\mathbf{E}_c$ in a frequency interval $[0.99\ 1.01] \times f_i$. We calculate the phase shift $\Delta\Phi$ at this frequency by interpolating the values from the numerical relations shown in Figure 2b. If a component has $\Delta\Phi > \pi$ the sign of this component is incorrect, and we correct it by flipping its sign.
   - To the filtered signal obtained above, we apply a minimum variance analysis in order to obtain the maximum variance direction $\mathbf{M}$, which corresponds to the direction of propagation for electrostatic waves. As $\mathbf{M}$ has a π ambiguity, we choose its sign such that its spin-plane component is aligned with $\vec{\kappa}$.
3. Calculate the 3D wave vector ($\mathbf{k}$) at each frequency:
   - We calculate the angle between $\mathbf{M}$ and the axial direction θ_{kz} and assume that it corresponds to the angle that $\mathbf{k}$ makes with the axial direction.
   - We construct the 3D wave vector by using $\vec{\kappa}$ for the spin-plane components and determining the axial component using

$$k_z = \left(k_x^2 + k_y^2\right)^{(1/2)} \frac{\cos(\theta_{kz})}{\sin(\theta_{kz})} \tag{8}$$

So, the final wave vector becomes $\mathbf{k}(f_i) = \left[\vec{\kappa}(f_i),\ k_z(f_i)\right]$.

In following those steps, we assume that the electric field in the axial direction is not subject to short-wavelength attenuation or phase shift. To check how well the method works, and to what extent those assumptions hold, we apply it to synthetic data of the wave packet described in Section 3.1, we plot in Figure 6a the angle between the measured and the theoretical wave vectors θ_{rm} and in panel (b) the ratio between the theoretical and measured wavelength $R = \lambda_t/\lambda_m$ of the same wave burst analyzed in Figure 5. For small frequencies (large wavelengths) (<800 Hz) $\theta_{rm} < 2°$ and $R \approx 1$ showing that for this frequency range the method works well in measuring the 3D wave vector (both direction and magnitude) where both assumptions made are valid. As the wavelength approaches the probe-to-probe separation (and its integer fraction, $\lambda = d_{ij}/n$ where n is an integer) the method slightly overestimates the wavelength with $R \sim 0.9$, while greatly deviates when it comes to the direction of propagation with $\theta_{rm} \sim 50°$.

To check what range in parameter space (all combinations of the triplet (λ, θ, ϕ)) we expect the method to work we run the simulation above by varying the polar angle θ of the wave packet in the range $[0\ 180]°$ and the azimuthal angle ϕ in the range $[-180\ 180]°$ with an angular resolution of $1°$. For each combination of the triplet (λ, θ, ϕ), we calculate R and θ_{rm}. For a fixed polar angle of $\theta = 60°$, we plot θ_{rm} in panel (c) and R in panel (d). We see that for all wavelengths larger than 120 m the method works fine in measuring the full 3D wave vector where $\theta_{rm} < 2°$ and $R \sim 1$. For wavelengths shorter than 120 m, the measured direction of propagation deviates from the theoretical direction of propagation with θ_{rm} reaching $60°$ while the wavelength is only slightly overestimated with R having a minimum value of 0.8. This occurs only at combinations of (λ, θ, ϕ) where the projection of λ on the direction of one of the probes is close to the probe-to-probe separation and its integer fraction (LaBelle & Kintner, 1989). At such values α in that direction would be close to zero, and the method fails since we are dividing by it to correct for the electric field.

3.3. 3D Wave Vector Determination: The Inverse Problem

The results in the previous subsection are informative but when the method is applied to real data one cannot know a priori if the waves are in a parameter range where the method is expected to work or not. We use the simulation data to develop a look-up table which we use to determine the 3D wave vector of any measured electrostatic wave burst. We know that we have five independent observables:

1. the measured wavelength of the wave λ_m,
2. the polar angle of the measured wave vector θ_{km},
3. the azimuthal angle of the measured wave vector ϕ_{km},
4. the polar angle of the uncorrected electric field θ_{Eu}, and
5. the azimuthal angle of the uncorrected electric field ϕ_{Eu}.
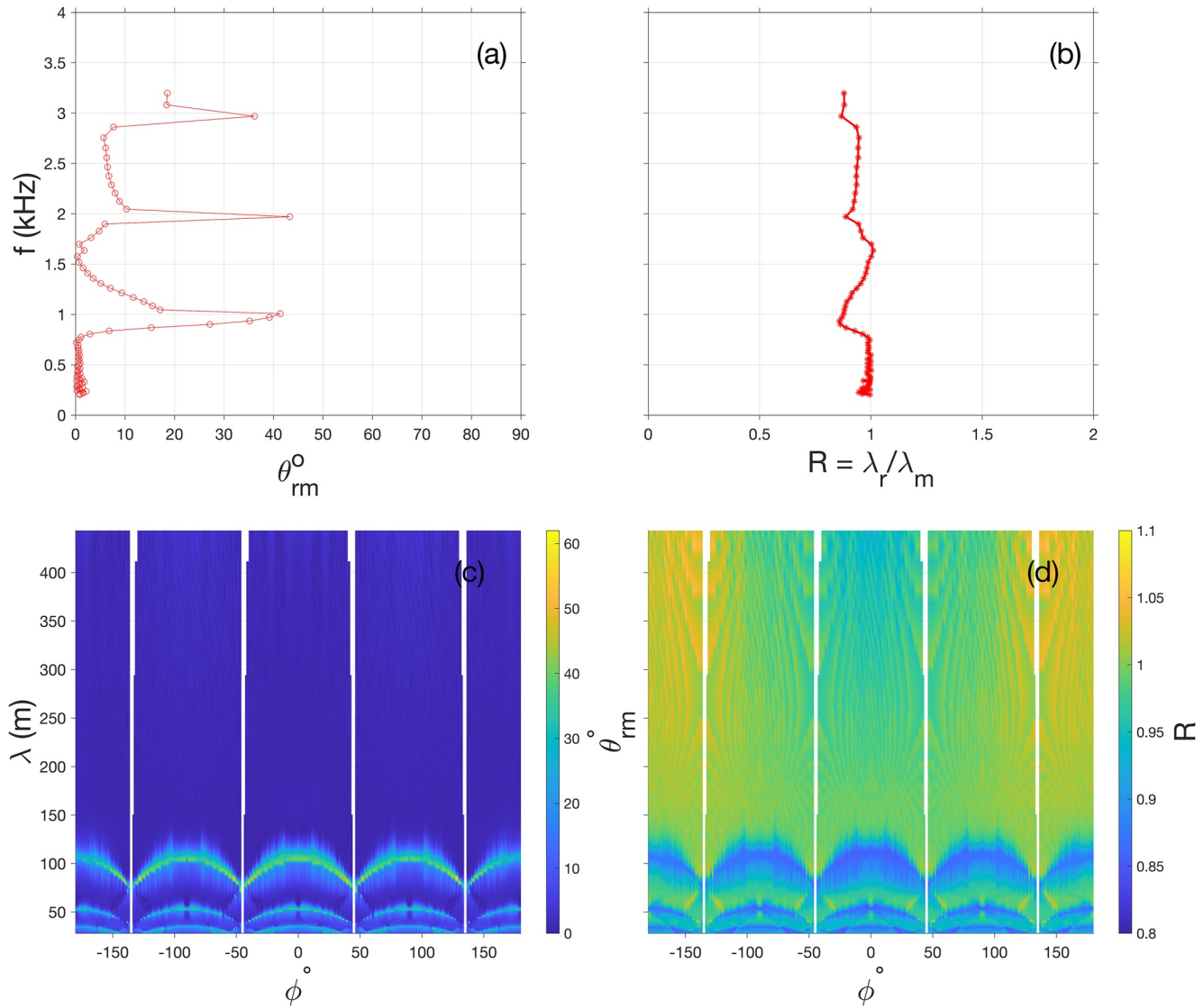
Figure 6. Comparing measured and theoretical properties of the synthetic waves. Panels (a) and (b) show the angle between the measured and the theoretical wave vectors θ_{rm} and the ratio between the theoretical and measured wavelength $R = \lambda_r/\lambda_m$, respectively, for the wave modeled in Figure 5. Panels (c) and (d) show a surface plot of the wavelength λ versus the azimuthal angle ϕ for waves propagating at a polar angle $\theta_z = 60°$, with the colorbars representing θ_{rm} and R, respectively.

We then ask the question: what simulated plane wave characterized by the triplet (λ, θ, ϕ) would give us values of the five observables that are closest to what we measure from the real wave. We then search for solutions that satisfy the following conditions:

$$|\Delta\lambda_m| = |\lambda_{m-dat} - \lambda_{m-sim}| \leq 5m$$

$$|\Delta\theta_m| = |\theta_{km-dat} - \theta_{km-sim}| \leq 5°$$

$$|\Delta\phi_m| = |\phi_{km-dat} - \phi_{km-sim}| \leq 5° \tag{9}$$

$$|\Delta\theta_{Eu}| = |\theta_{Eu-dat} - \theta_{Eu-sim}| \leq 10°$$

$$|\Delta\phi_{Eu}| = |\phi_{Eu-dat} - \phi_{Eu-sim}| \leq 10°$$

Multiple triplet combinations satisfy equation. We apply this calculation to the simulated wave packet whose potential is described by Equation 7 with white noise with signal-to-noise ratio of 15 dB added to simulate real waves measurement. Figure 7a shows f versus θ_{kB}, while panel (b) is a plot of the f versus λ. In both panels, the blue stars are the values corresponding to all solutions of the system of equations at each frequency component, the black line is the
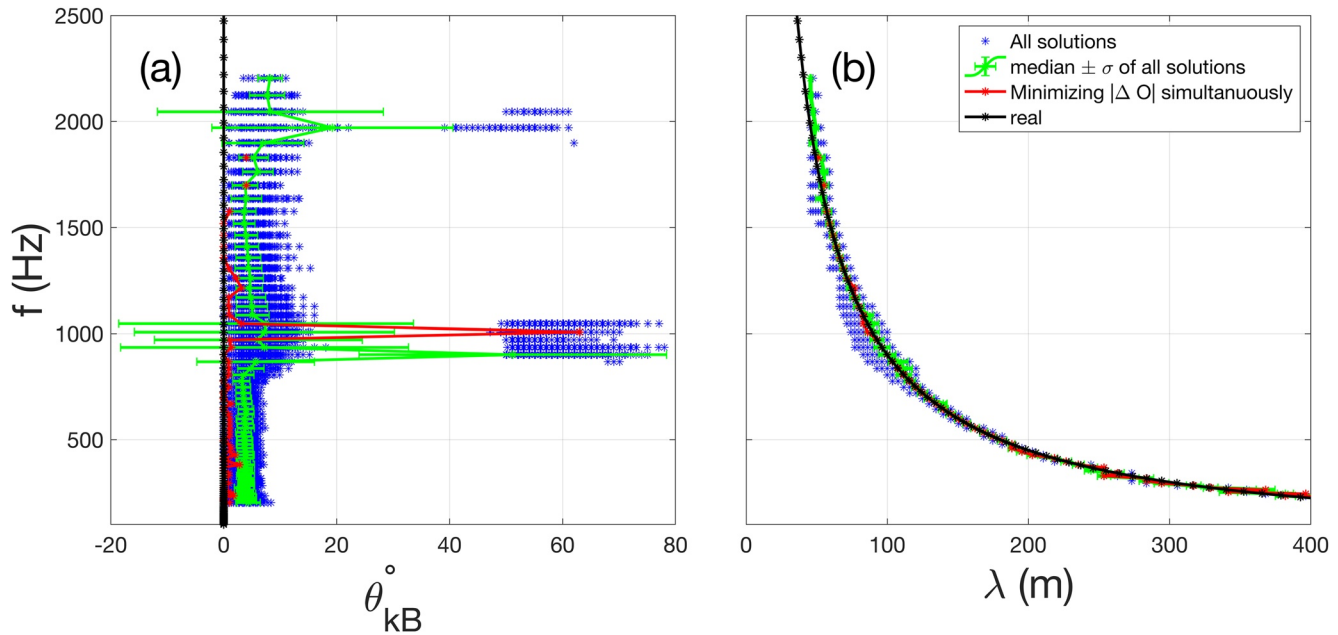
Figure 7. Solutions to the inverse problem. Panels (a) and (b) show the frequency versus θ_{kB} and frequency versus λ, respectively. Blue stars are all the waves that solve the set of five equations, black line represent the real values, red are the results of finding the one solution that minimizes the set of five equations simultaneously and green error bar represent the median and standard deviation of all solutions.

expected values of θ_{kB}/λ, the red line shows the values that minimize all five equations simultaneously, and the green error bars represent the median and standard deviation of all solutions at each frequency. The solution that minimizes all quantities simultaneously (red curves) does a good job at retrieving the dispersion relation, but at some points it deviates from the true properties of the wave (it predicts a $\theta_{kB} \sim 60°$ at $f \sim 1$ KHz). So instead the final output of the method and what we report as our final measurement for the wave properties will be the median of all the solutions at each frequency component and we take the standard deviation of all solutions as an error estimate on this measurement (green error bar). As is clear from panels (c and d) of Figure 6, below a wavelength of ~50 m, the integer fraction of the wavelength where the method fails becomes closer to each other. Also, from Figure 2, it is clear that the assumption that the axial component of the electric field is not subject to attenuation fails. That is why we limit the simulation to wavelength larger than 45 m and take that value as the minimum wavelength that we can resolve.

In developing this method, we neglected any corrections in amplitudes due to sheath impedance or boom shorting effects. The usual way to correct the electric field is by multiplying it by gain factors corresponding to each effect. Those gain factors are dependent on the properties of the wave and plasma environment (density and frequency). The ratio between the axial and spin-plane gain factors (r_{sheath} for sheath impedance and r_{short} for boom shorting) affect the value of θ_{Ez} that we use to get the 3D wave vector in our method. For the sheath impedance effect, the burst data products that we use are precalibrated using transfer functions obtained from ground calibration (Khotyaintsev et al., 2017) so $r_{sheath} \sim 1$. As for the boom shorting effect, it is most severe in the solar wind where the Debye length is large and becomes less effective as the Debye length decrease (density of the plasma increase). The value of r_{short} used to correct the electric field by the EDP team is ~1.4 obtained from calibration done on DC fields mainly in magnetosheath and magnetosphere. Using this estimate for r_{short}, we determine that ignoring the shorting effect can add a maximum of ~10° uncertainty to our measurement. We expect the error to be smaller in the solar wind as the Debye length there is generally shorter than the region where the calibration has been performed and thus the effective length would be closer to the physical length. Furthermore, the excellent agreement between the observed and synthetic θ_{Ez} distributions with the latter obtained by accounting for the short-wavelength effect only shown (Figure 3d) shows that this is the dominant effect and the errors introduced by other effects are small.

3.4. 3D Wave Vector Determination: Spacecraft Data

Now that we developed the method on synthetic data, we apply it to the wave burst measured by MMS1 shown in Figure 1. In panel (a) of Figure 8, we plot the uncorrected electric field showing that the amplitude of the z
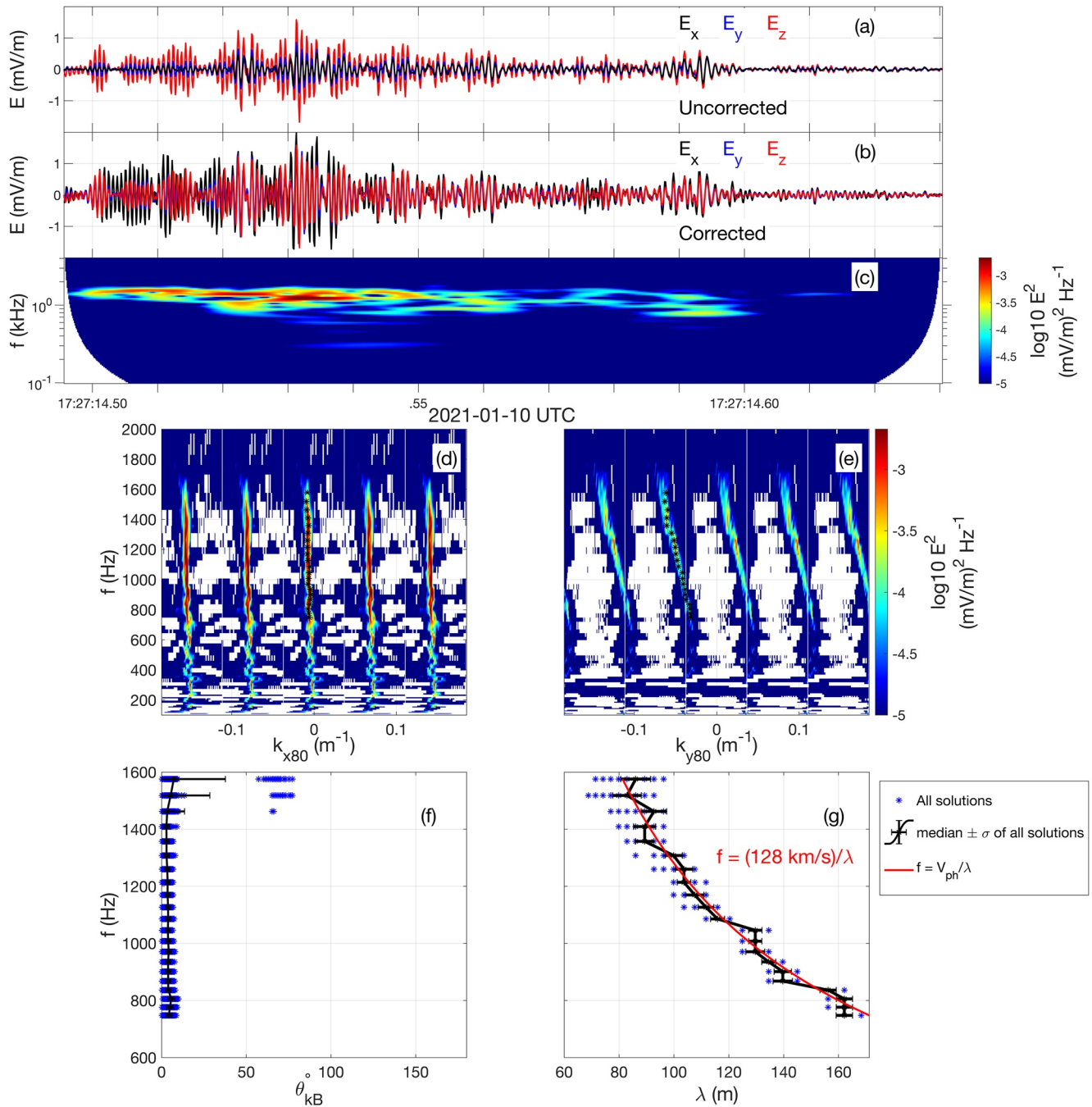
Figure 8. Application of the method to the wave burst in Figure 1. Panel (a) shows the uncorrected electric field in the probes coordinate system (PCS), (b) corrected electric field, (c) corrected electric field PSD, (d and e) $f − k$ power spectral density (PSD) in the x_{80} and y_{80} directions, respectively. Panels (f) and (g) show the result of the method, where frequency versus θ_{kB} is plotted in (f) and versus λ (g). Blue stars are all solutions matching the observables, black error bar represents the median and standard deviation of those solutions. The red curve in panel (g) represents a weighted fit to the equation $f = V_{ph}/\lambda$, of the data with the standard deviation as the weights.

component of the electric field is significantly larger than that in the spin plane (x, y). Panel (b) shows electric field after correcting for the attenuation, using the method described above, in the spin plane. As is clear, the spin-plane components of the electric field have now comparable amplitude to that in the axial direction. Panel (c) shows the corrected electric field PSD. Panels (d) and (e) show the $f − k$ PSD in the x_{80} and y_{80} directions showing a linear dispersion relation. As before, we choose the branches that connect to the origin and highlight them with the black stars.

Panel (f) shows the frequency versus θ_{kB}, while panel (g) shows the frequency versus the wavelength, with least square fits to the function $f = V_{ph}/\lambda$ overlayed in red. On top of the measurement of the dispersion relation in panel (g), we clearly see in panel (f) that this wave burst is not oblique and travels in the field-aligned direction with $\theta_{kB} \sim 3°$. This can be compared to $\theta_{kB} \sim 31°$ obtained using the maximum variance direction of the uncorrected electric field. It is worth noting that at higher frequencies two different clusters of solutions are visible in panel (f), the first have $\theta_{kB} \sim 3°$ and the second around $70°$. The error bars for those frequencies are significantly larger compared to the other frequencies, as they should be, reflecting the extra uncertainty that the second cluster of solutions add to our measurement.

4. Properties of Ion Acoustic Waves in the Solar Wind

In this section, we use the method developed above to investigate the properties of the solar wind ion acoustic wave bursts. First, we look at an event where the wave burst exhibits interesting behavior in its wavelet spectrum. Second, we perform a statistical study of the properties of ion acoustic waves in the solar wind.

4.1. Case Study

Several wave bursts in our list exhibit an interesting behavior in their PSD where what seems to be a continuous waveform in the time domain, exhibits a discontinuity in the wavelet domain. An example is shown in Figure 9. Panel (a) shows the uncorrected electric field featuring an increasing amplitude peaking at around 5 mV/m then decreasing with what looks like a wave trail. Panel (b) shows the corrected electric field showing that the lower amplitude wave trail is nothing but part of the higher frequency component of the wave burst which is subject to great attenuation in amplitude. Panel (c) shows the corrected electric field PSD which shows that what seems to be one wave burst has two disconnected PSD signatures one at lower frequency and the other at higher frequency. Panels (d) and (e) show the $f - k$ PSD in the x_{80} and y_{80} directions again showing the signature of two separate dispersion relations (which looks nonlinear).

Panels (f and g) show the wave properties obtained for this wave burst. Panel (f) shows the frequency versus θ_{kB}, while panel (g) shows the frequency versus the wavelength, with least square fits to the function $f = V_{ph}/\lambda$ overlayed. The green fit is for the higher frequency component of the dispersion relation while the red fit is for the lower frequency component. We can clearly see that the lower frequency component of the wave burst travel at a more oblique angle ($\theta_{kB} \approx 130°$) and with slower phase velocity ($V_{ph} = 143$ km/s) in the spacecraft frame, compared to the higher frequency component travel which is more antifield aligned ($\theta_{kB} \approx 150°$) and at higher phase velocity ($V_{ph} = 233$ km/s). If we Doppler shift the dispersion relation to the plasma frame (not shown), we see that the two disconnected components become one continuous dispersion relation. This means that due to the different direction of propagation the two wave bursts appear discontinuous in the spacecraft frame.

4.2. Statistical Study

From the previously compiled 210 wave bursts, only 105 show a clear dispersive character in the spin plane allowing us to apply the method. For each of those events, we apply the method and fit the resulting dispersion relation to the equation $f = V_{ph}/\lambda$. To insure that the data properly fit the dispersion relation, we use the parameter R-squared $= 1 - \frac{\sum_i (y_i - f_i)^2}{\sum_i (y_i - \bar{y})^2}$ to assess the goodness of the fit. In the formula for R-squared, y_i is the ith measured value of the dependent variable y corresponding to the ith measured value of the independent variable x in the fit, f_i is the value of the fit evaluated at x_i and $\bar{y}$ is the mean value of y_i. The closer R-squared is to 1, the better the fit is. We discard all events whose fits have an R-squared value <0.1 (i.e., the measured dispersion relation does not fit the function $f = V_{ph}/\lambda$ properly), which leaves us with a total of 48 events. For each of those 48 events, we find the frequency value which corresponds to the peak power. The interpolated λ and θ_{kB} at that frequency are then taken as the representative values for each wave burst.

In Figure 10, we plot the histogram of the results. Panel (a) shows the distribution of θ_{kB}. We retrieve the expected result that ion acoustic waves in the solar wind are predominantly field aligned. In panel (b), we show the statistical distribution of the wavelength of ion acoustic waves in the solar wind. The distribution peaks at around 100 m consistent with previous measurements (Gurnett & Frank, 1978). Panels (c and d) show the distribution of wavelengths normalized to λ_D and f_{pi}/C_s, respectively, where f_{pi} is the measured ion plasma frequency and C_s
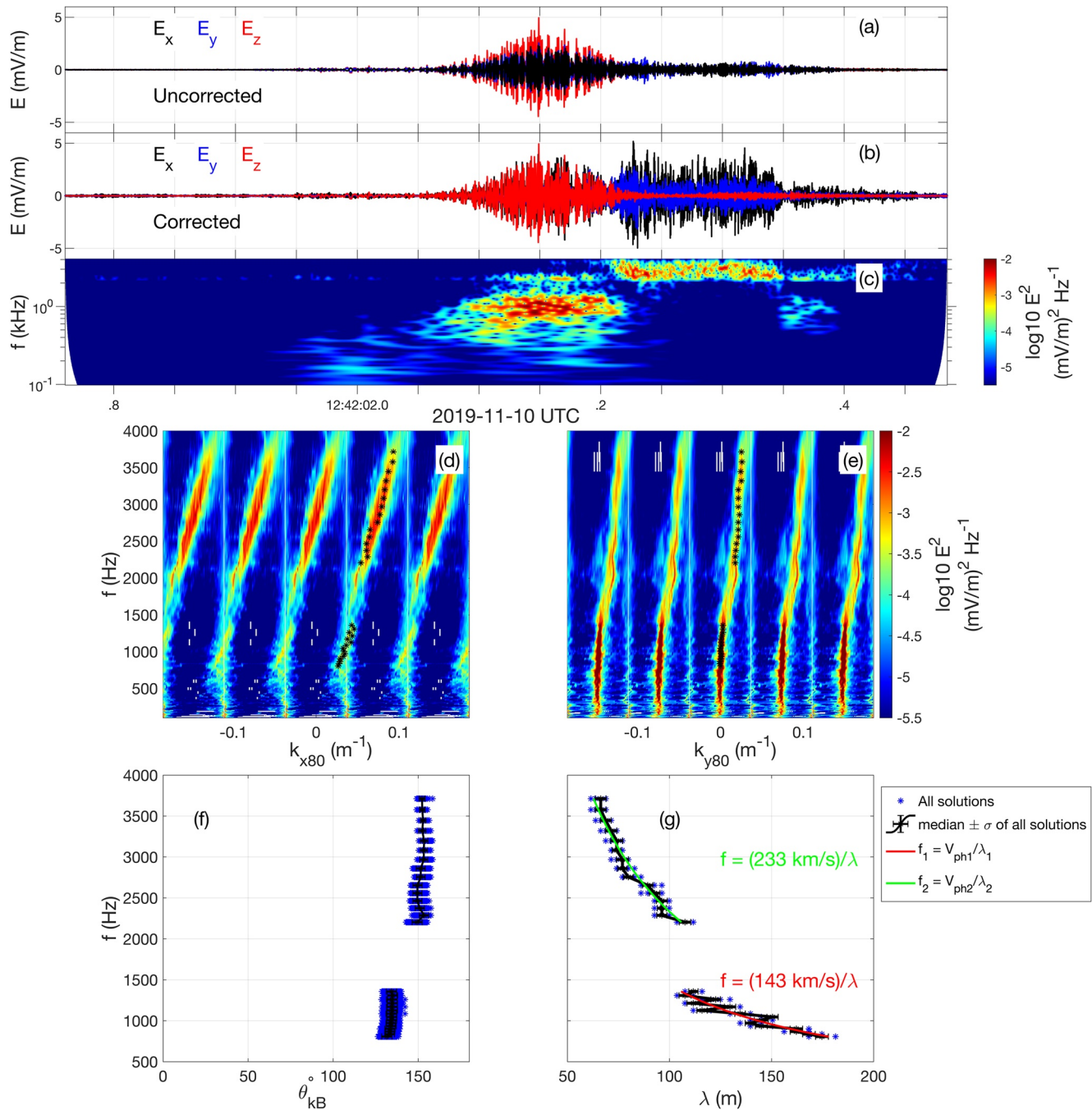
Figure 9. Wave burst showing a discontinuity in its power spectral density (PSD) along with the measured dispersion relation. Same format as in Figure 8.

is the measured ion sound speed (as defined earlier). The ratio f_{pi}/C_s can be taken as a characteristic wavelength for ion acoustic waves. The measured distribution peaks between 10 and 20 λ_D or between 1 and 2 f_{pi}/C_s, which is consistent with theoretical expectations.

5. Conclusion

Characterization of high-frequency short-wavelength electrostatic waves requires reliable measurement of the wave electric field along with the determination of the wave vector. We observe that the electric field of ion acoustic waves measured by MMS in the solar wind is systematically biased toward the axial (approximately
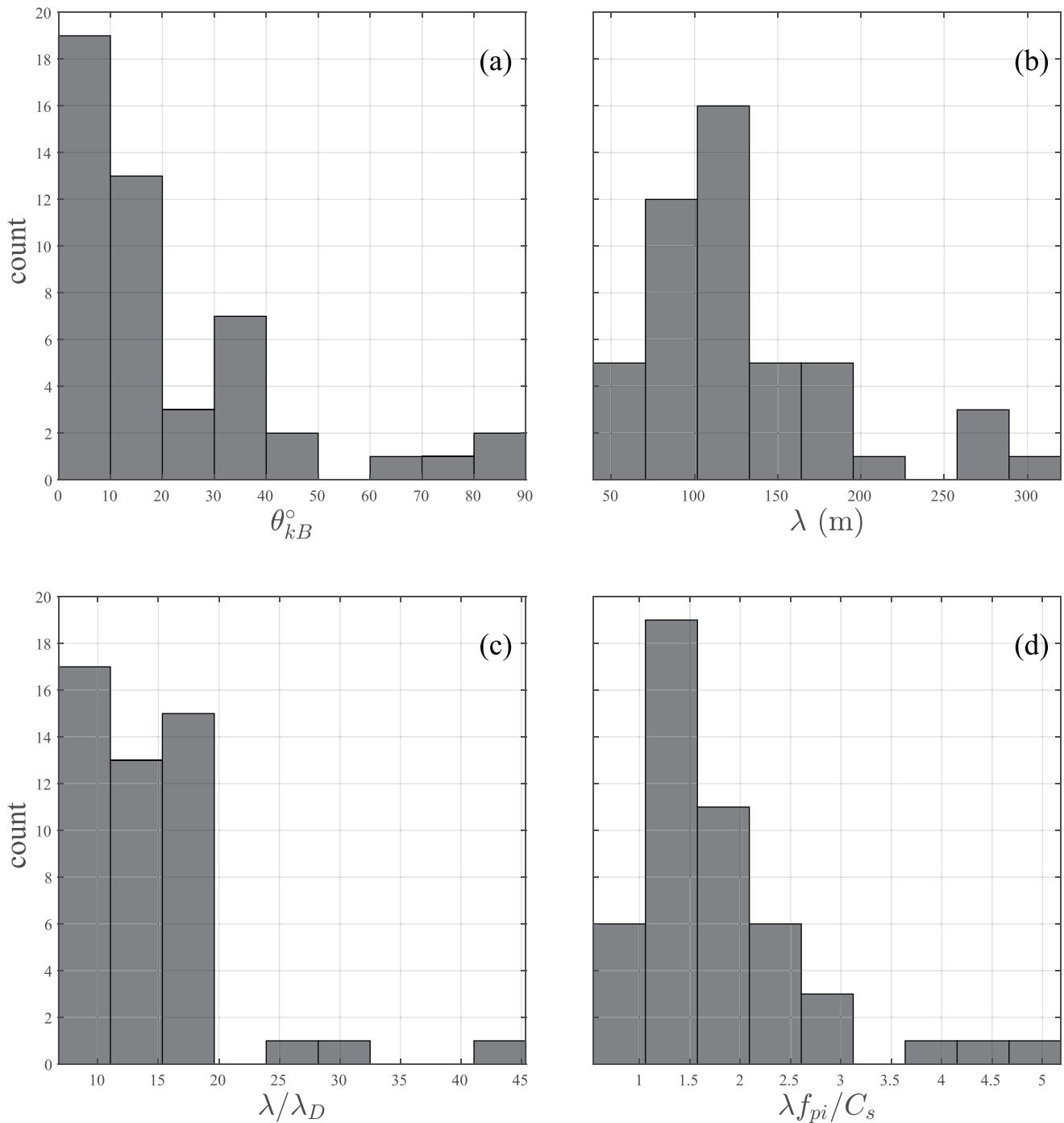
Figure 10. Statistical properties of ion acoustic waves in the solar wind. Panel (a) is a histogram of θ_{kB}, (b) histogram of the wavelength λ, (c) histogram of the wavelength normalized to the Debye length λ/λ_D, and (d) histogram of the wavelength normalized to f_{pi}/C_s with f_{pi} being the measured ion plasma frequency and C_s the measured sound speed.

GSE Z) direction. A similar problem has been identified for the high-frequency waves at the shock (Goodrich et al., 2018; Vasko et al., 2018; Wang et al., 2021). This bias makes it difficult to determine the wave mode using the measured electric field.

We show that this bias is caused by the electric field measured by the double-probe instrument being attenuated when the wavelength of the waves approaches the probe-to-probe separation (short-wavelength effect). To address this problem, we develop a method to measure the 3D wave vector of an electrostatic wave. The method

is based on spin-plane interferometry, it assumes that we are measuring plane waves with wavelength larger than 45 m (1.5 times separation of the axial probes, and 0.37 times that of the spin-plane probes) and propagating at an angle to the axial direction so that there is a significant signal in the spin-plane measurement. We benchmark this method on both synthetic data and real data whose properties are generally known, namely ion acoustic waves measured in the solar wind. Previous statistical analysis of solar wind ion acoustic waves was done using 2D measurements of the electric field. Instead, our method allows us to determine the full 3D wave vector of the waves for the first time. We find that the waves travel predominantly in the field-aligned direction (well-known result), and have a wavelength of ~100 m or 10 to 20 Debye lengths.

The proposed method can be applied to study short-wavelength electrostatic waves (wavelength >45 m), which often occur in the near-Earth regions with sufficiently short Debye lengths encountered by MMS, particularly at the bow shock, magnetosheath, and magnetopause.

Data Availability Statement

MMS data are available at https://lasp.colorado.edu/mms/sdc/public/data/. Data analysis was performed using the IRFU-Matlab analysis package. The code for applying the method developed in this paper along with the code to generate the simulation data can be found at https://github.com/ahmadlalti/ESW-measurement.git. The simulation data can be found at https://doi.org/10.5281/zenodo.7682439.

References

Balikhin, M., Walker, S., Treumann, R., Alleyne, H., Krasnoselskikh, V., Gedalin, M., et al. (2005). Ion sound wave packets at the quasiperpendicular shock front. *Geophysical Research Letters*, *32*, L24106. https://doi.org/10.1029/2005GL024660

Baumjohann, W., & Treumann, R. A. (2012). *Basic space plasma physics*. World Scientific.

Bonnell, J., Kintner, P., Wahlund, J. E., Lynch, K., & Arnoldy, R. (1996). Interferometric determination of broadband ELF wave phase velocity within a region of transverse auroral ion acceleration. *Geophysical Research Letters*, *23*(23), 3297–3300. https://doi.org/10.1029/96GL03238

Bonnell, J., Mozer, F., Delory, G., Hull, A., Ergun, R., Cully, C., et al. (2009). The electric field instrument (EFI) for themis. In *The themis mission* (pp. 303–341). Springer.

Burch, J., Moore, T., Torbert, R., & Giles, B. (2016). Magnetospheric multiscale overview and science objectives. *Space Science Reviews*, *199*(1–4), 5–21. https://doi.org/10.1007/s11214-015-0164-9

Califf, S., & Cully, C. M. (2016). Empirical estimates and theoretical predictions of the shorting factor for the THEMIS double-probe electric field instrument. *Journal of Geophysical Research: Space Physics*, *121*, 6223–6233. https://doi.org/10.1002/2016JA022589

Ergun, R., Tucker, S., Westfall, J., Goodrich, K., Malaspina, D., Summers, D., et al. (2016). The axial double probe and fields signal processing for the mms mission. *Space Science Reviews*, *199*(1), 167–188. https://doi.org/10.1007/s11214-014-0115-x

Fahleson, U. (1967). Theory of electric field measurements conducted in the magnetosphere with electric probes. *Space Science Reviews*, *7*(2–3), 238–262. https://doi.org/10.1007/BF00215600

Goodrich, K. A., Ergun, R., Schwartz, S. J., Wilson, L. B., Newman, D., Wilder, F. D., et al. (2018). MMS observations of electrostatic waves in an oblique shock crossing. *Journal of Geophysical Research: Space Physics*, *123*, 9430–9442. https://doi.org/10.1029/2018JA025830

Graham, D. B., Khotyaintsev, Y. V., André, M., Vaivads, A., Divin, A., Drake, J. F., et al. (2022). Direct observations of anomalous resistivity and diffusion in collisionless plasma. *Nature Communications*, *13*(1), 2954. https://doi.org/10.1038/s41467-022-30561-8

Graham, D. B., Khotyaintsev, Y. V., Vaivads, A., & André, M. (2016). Electrostatic solitary waves and electrostatic waves at the magnetopause. *Journal of Geophysical Research: Space Physics*, *121*, 3069–3092. https://doi.org/10.1002/2015JA021527

Gurnett, D. A. (1991). Waves and instabilities. In *Physics of the inner heliosphere II* (pp. 135–157). Springer.

Gurnett, D. A. (1998). *Principles of space plasma wave instrument design* (Vol. 103, pp. 121–136). Geophysical Monograph-American Geophysical Union.

Gurnett, D. A., & Anderson, R. R. (1977). Plasma wave electric fields in the solar wind: Initial results from helios 1. *Journal of Geophysical Research*, *82*(4), 632–650. https://doi.org/10.1029/JA082i004p00632

Gurnett, D. A., & Frank, L. A. (1978). Ion acoustic waves in the solar wind. *Journal of Geophysical Research*, *83*(A1), 58–74. https://doi.org/10.1029/JA083iA01p00058

Gustafsson, G., Boström, R., Holback, B., Holmgren, G., Lundgren, A., Stasiewicz, K., et al. (1997). The electric field and wave experiment for the cluster mission. *Space Science Reviews*, *79*(1), 137–156. https://doi.org/10.1023/a:1004975108657

Hartley, D., Kletzing, C., Kurth, W., Bounds, S., Averkamp, T., Hospodarsky, G., et al. (2016). Using the cold plasma dispersion relation and whistler mode waves to quantify the antenna sheath impedance of the Van Allen probes efw instrument. *Journal of Geophysical Research: Space Physics*, *121*, 4590–4606. https://doi.org/10.1002/2016JA022501

Khotyaintsev, Y., Lindqvist, P.-A., & Nilsson, T. (2017). Spin-plane double probe instrument/axial double probe instrument (SDP/ADP) data products guide (Tech. Rep.). IRFU/KTH. Retrieved from https://lasp.colorado.edu/mms/sdc

Khotyaintsev, Y. V., Graham, D. B., Norgren, C., & Vaivads, A. (2019). Collisionless magnetic reconnection and waves: Progress review. *Frontiers in Astronomy and Space Sciences*, *6*, 70. https://doi.org/10.3389/fspas.2019.00070

Khotyaintsev, Y. V., Graham, D. B., Steinvall, K., Alm, L., Vaivads, A., Johlander, A., et al. (2020). Electron heating by Debye-scale turbulence in guide-field reconnection. *Physical Review Letters*, *124*(4), 045101. https://doi.org/10.1103/PhysRevLett.124.045101

Khotyaintsev, Y. V., Vaivads, A., André, M., Fujimoto, M., Retinò, A., & Owen, C. J. (2010). Observations of slow electron holes at a magnetic reconnection site. *Physical Review Letters*, *105*(16), 165002. https://doi.org/10.1103/PhysRevLett.105.165002

LaBelle, J., & Kintner, P. (1989). The measurement of wavelength in space plasmas. *Reviews of Geophysics*, *27*(4), 495–518. https://doi.org/10.1029/rg027i004p00495

Le Contel, O., Nakamura, R., Breuillard, H., Argall, M. R., Graham, D. B., Fischer, D., et al. (2017). Lower hybrid drift waves and electromagnetic electron space-phase holes associated with dipolarization fronts and field-aligned currents observed by the magnetospheric multiscale mission during a substorm. *Journal of Geophysical Research: Space Physics*, *122*, 12236–12257. https://doi.org/10.1002/2017JA024550

Lindqvist, P.-A., Olsson, G., Torbert, R., King, B., Granoff, M., Rau, D., et al. (2016). The spin-plane double probe electric field instrument for mms. *Space Science Reviews*, *199*(1), 137–165. https://doi.org/10.1007/s11214-014-0116-9

Maksimovic, M., Bale, S., Chust, T., Khotyaintsev, Y., Krasnoselskikh, V., Kretzschmar, M., et al. (2020). The solar orbiter radio and plasma waves (RPW) instrument. *Astronomy & Astrophysics*, *642*, A12. https://doi.org/10.1051/0004-6361/201936214

Mozer, F. (1973). Analyses of techniques for measuring dc and ac electric fields in the magnetosphere. *Space Science Reviews*, *14*(2), 272–313. https://doi.org/10.1007/bf02432099

Mozer, F., Bonnell, J., Bowen, T., Schumm, G., & Vasko, I. (2020). Large-amplitude, wideband, Doppler-shifted, ion acoustic waves observed on the parker solar probe. *The Astrophysical Journal*, *901*(2), 107. https://doi.org/10.3847/1538-4357/abafb4

Mozer, F., & Bruston, P. (1967). Electric field measurements in the auroral ionosphere. *Journal of Geophysical Research*, *72*(3), 1109–1114. https://doi.org/10.1029/jz072i003p01109

Paschmann, G., & Daly, P. W. (1998). *Analysis methods for multi-spacecraft data*. The International Space Science Institute.

Pedersen, A., Mozer, F., & Gustafsson, G. (1998). Electric field measurements in a tenuous plasma with spherical double probes. *Geophysical Monograph-American Geophysical Union*, *103*, 1–12.

Píša, D., Souček, J., Santolík, O., Hanzelka, M., Nicolaou, G., Maksimovic, M., et al. (2021). First-year ion-acoustic wave observations in the solar wind by the RPW/TDS instrument on board solar orbiter. *Astronomy & Astrophysics*, *656*, A14. https://doi.org/10.1051/0004-6361/202140928

Richard, L., Khotyaintsev, Y. V., Graham, D. B., Sitnov, M. I., Le Contel, O., & Lindqvist, P. A. (2021). Observations of short-period ion-scale current sheet flapping. *Journal of Geophysical Research: Space Physics*, *126*, e29152. https://doi.org/10.1029/2021JA029152

Sagdeev, R. (1966). Cooperative phenomena and shock waves in collisionless plasmas. *Reviews of Plasma Physics*, *4*, 23.

Sonnerup, B. U. Ö., & Scheible, M. (1998). Minimum and maximum variance analysis. *ISSI Scientific Reports Series*, *1*, 185–220.

Steinvall, K., Khotyaintsev, Y. V., & Graham, D. B. (2022). On the applicability of single-spacecraft interferometry methods using electric field probes. *Journal of Geophysical Research: Space Physics*, *127*, e2021JA030143. https://doi.org/10.1029/2021JA030143

Steinvall, K., Khotyaintsev, Y. V., Graham, D. B., Vaivads, A., Le Contel, O., & Russell, C. T. (2019). Observations of electromagnetic electron holes and evidence of Cherenkov whistler emission. *Physical Review Letters*, *123*(25), 255101. https://doi.org/10.1103/PhysRevLett.123.255101

Vaivads, A., André, M., Buchert, S. C., Wahlund, J. E., Fazakerley, A. N., & Cornilleau-Wehrlin, N. (2004). Cluster observations of lower hybrid turbulence within thin layers at the magnetopause. *Geophysical Research Letters*, *31*, L03804. https://doi.org/10.1029/2003GL018142

Valentini, F., Vecchio, A., Donato, S., Carbone, V., Briand, C., Bougeret, J., & Veltri, P. (2014). The nonlinear and nonlocal link between macroscopic alfvénic and microscopic electrostatic scales in the solar wind. *The Astrophysical Journal Letters*, *788*(1), L16. https://doi.org/10.1088/2041-8205/788/1/l16

Valentini, F., & Veltri, P. (2009). Electrostatic short-scale termination of solar-wind turbulence. *Physical Review Letters*, *102*(22), 225001. https://doi.org/10.1103/PhysRevLett.102.225001

Valentini, F., Veltri, P., Califano, F., & Mangeney, A. (2008). Cross-scale effects in solar-wind turbulence. *Physical Review Letters*, *101*(2), 025006. https://doi.org/10.1103/PhysRevLett.101.025006

Vasko, I. Y., Mozer, F. S., Bale, S. D., & Artemyev, A. V. (2022). Ion-acoustic waves in a quasi-perpendicular Earth's bow shock. *Geophysical Research Letters*, *49*, e2022GL098640. https://doi.org/10.1029/2022GL098640

Vasko, I. Y., Mozer, F. S., Krasnoselskikh, V. V., Artemyev, A. V., Agapitov, O. V., Bale, S. D., et al. (2018). Solitary waves across supercritical quasi-perpendicular shocks. *Geophysical Research Letters*, *45*, 5809–5817. https://doi.org/10.1029/2018GL077835

Wang, R., Vasko, I., Mozer, F., Bale, S., Kuzichev, I., Artemyev, A., et al. (2021). Electrostatic solitary waves in the Earth's bow shock: Nature, properties, lifetimes, and origin. *Journal of Geophysical Research: Space Physics*, *126*, e2021JA029357. https://doi.org/10.1029/2021JA029357

Wilson, L. B., III, Brosius, A. L., Gopalswamy, N., Nieves-Chinchilla, T., Szabo, A., Hurley, K., et al. (2021). A quarter century of wind spacecraft discoveries. *Reviews of Geophysics*, *59*, e2020RG000714. https://doi.org/10.1029/2020RG000714

Wilson, L. B., Sibeck, D. G., Breneman, A. W., Le Contel, O., Cully, C., Turner, D. L., et al. (2014a). Quantified energy dissipation rates in the terrestrial bow shock: 1. Analysis techniques and methodology. *Journal of Geophysical Research: Space Physics*, *119*, 6455–6474. https://doi.org/10.1002/2014JA019929

Wilson, L. B., Sibeck, D. G., Breneman, A. W., Le Contel, O., Cully, C., Turner, D. L., et al. (2014b). Quantified energy dissipation rates in the terrestrial bow shock: 2. Waves and dissipation. *Journal of Geophysical Research: Space Physics*, *119*, 6475–6495. https://doi.org/10.1002/2014JA019930

Wygant, J., Bonnell, J., Goetz, K., Ergun, R., Mozer, F., Bale, S., et al. (2013). The electric field and waves instruments on the radiation belt storm probes mission. In *The Van Allen probes mission* (pp. 183–220). Springer.